Inhibitor-induced structural change in the HCV IRES domain IIa RNA

Ryan B. Paulsen[a], Punit P. Seth[b], Eric E. Swayze[b], Richard H. Griffey[b], Jack J. Skalicky[c], Thomas E. Cheatham III[a,d], and Darrell R. Davis[a,c,1]

[a]Department of Medicinal Chemistry,[c]Department of Biochemistry, and[d]Department of Pharmaceutics and Pharmaceutical Chemistry, University of Utah, Salt Lake City, UT 84112; [b]Isis Pharmaceuticals Inc., 1891 Rutherford Road, Carlsbad, CA 92008

Edited by Dinshaw J. Patel, Memorial Sloan-Kettering Cancer Center, New York, NY, and approved March 1, 2010 (received for review October 14, 2009)

Translation of the hepatitis C virus (HCV) RNA is initiated from a highly structured internal ribosomal entry site (IRES) in the 5′ untranslated region (5′ UTR) of the RNA genome. An important structural feature of the native RNA is an approximately 90° helical bend localized to domain IIa that positions the apical loop of domain IIb of the IRES near the 40S ribosomal E-site to promote eIF2-GDP release, facilitating 80S ribosome assembly. We report here the NMR structure of a domain IIa construct in complex with a potent small-molecule inhibitor of HCV replication. Molecular dynamics refinement in explicit solvent and subsequent energetic analysis indicated that each inhibitor stereoisomer bound with comparable affinity and in an equivalent binding mode. The in silico analysis was substantiated by fluorescence-based assays showing that the relative binding free energies differed by only 0.7 kcal/mol. Binding of the inhibitor displaces key nucleotide residues within the bulge region, effecting a major conformational change that eliminates the bent RNA helical trajectory, providing a mechanism for the antiviral activity of this inhibitor class.

antiviral | hepatitis C virus | molecular dynamics | RNA structure

Hepatitis C virus (HCV) is a positive-sense, single-stranded RNA *Hepacivirus* in the *Flaviviridae* family of which yellow-fever virus and dengue virus are closely related viral pathogens (1). HCV infection is a major public health problem with as many as 170 million people infected worldwide, and 2–3 million new cases per year. In western countries HCV infection causes the majority of cases of liver cancer, is the major cause of liver transplantations, and results in the death of approximately 10,000 people in the United States each year (2, 3). Upon viral entry, the initial phase of HCV replication involves polyprotein production via translation of the + strand genomic RNA. The 5′-UTR of the HCV genome/mRNA contains a large structured domain that serves as an internal ribosomal entry site (IRES). The IRES of HCV is among the best characterized, both structurally and functionally, of IRES elements from many different viruses and also of IRES elements found in cellular genes (4). Upon HCV infection, the normal cap-dependent translation process is strongly inhibited, and infected cells instead shift most of their protein synthesis capacity to viral polyprotein production. The HCV IRES element recruits the 40S ribosomal subunit directly to initiate viral RNA translation bypassing the requirement for several translation initiation factors. Domain II of the HCV IRES has a bent helical structure that is conserved in HCV and related viruses and appears to be crucial for the biological function of the IRES (5, 6). Domain II of the HCV IRES mediates the release of a key initiation factor, eIF2-GDP, from the 40S subunit to promote 80S ribosomal assembly (5, 7). Genetic analysis showed that the 5′ UTR for 83 of 124 HCV sequences could be folded into the consensus secondary structure shown schematically in Fig. 1*A* (8). Most of the variations found in the IRES sequences were conservative Watson–Crick base swaps that maintain the secondary structure of the stem regions and presumably result in a similar fold and overall structure.

A series of small-molecule HCV replication inhibitors with low micromolar affinities for domain IIa of the HCV IRES has been reported (9). The binding site of these compounds was localized to the conserved bulge region of domain IIa based on partial protection from RNase A digestion of residues C8 and U9 (Fig. 1*B*). Changes in RNase A reactivity for the bound state suggested inhibitor-bound structures might be significantly different, as is common in high-affinity RNA-ligand and RNA-protein interactions (10). A high-resolution structure of an inhibitor in this class, in complex with the HCV IRES RNA, would enable a structure-based drug design strategy to further increase the antiviral activity of these inhibitors. We have determined the structure for the most potent HCV inhibitor of this class in complex with an RNA hairpin containing the bend-inducing site of the HCV IRES domain II. NMR NOE- and residual dipolar coupling (RDC)-based structure determination using both standard Xplor refinement in vacuo and also more extensive AMBER molecular dynamics (MD) refinement in explicit solvent was done for each inhibitor stereoisomer. Subsequent energetic analysis suggested that both enantiomers bind with a similar affinity and mode to the RNA. The inhibitors induce a major structural change that removes the approximately 90° bend observed in the free RNA, providing a potential mechanism for the ability of these compounds to inhibit HCV replication. The inhibitor-bound form of the HCV IRES also provides a target for structure-based design of highly potent HCV therapeutics.

Results and Discussion

HCV IRES Inhibitor Binding to the Domain IIa Bulge. Domain IIa of the HCV IRES has an overall bent structure mediated by an internally stacked, five nucleotide bulge (11, 12) (Fig. 2*A*). In order to accommodate secondary structural rearrangements that may be necessary for specific binding of the Isis-11 inhibitor, our RNA construct for NMR study contained this bulge and the short region of four noncanonical base pairs from the native RNA. Residues 6, 7, and 8 in the free RNA structure stack on the G5–C34 base pair, resulting in a continuous helical arrangement of those three bulged nucleotides upon the lower stem. Accommodation of these nucleotides within the helix produces an approximately 90° bend in the helical axis that is thought to be crucial for IRES function (6, 7). The racemic inhibitor binds to the conserved bulge region, resulting in substantial NMR chemical shift changes for the protons of residues in this region (Fig. 2*B*). The 2D total

Author contributions: P.P.S., E.E.S., R.H.G., T.E.C., and D.R.D. designed research; R.B.P., P.P.S., J.J.S., and T.E.C. performed research; R.B.P., P.P.S., E.E.S., R.H.G., T.E.C., and D.R.D. analyzed data; and T.E.C. and D.R.D. wrote the paper.

The authors declare no conflict of interest.

This article is a PNAS Direct Submission.

Freely available online through the PNAS open access option.

Data deposition: The ensembles of 10 final structures for each isomer have been deposited in the Protein Data Bank (accession codes 2ktz and 2ku0).

[1]To whom correspondence should be addressed. E-mail: darrell.davis@utah.edu.

This article contains supporting information online at www.pnas.org/cgi/content/full/0911896107/DCSupplemental.

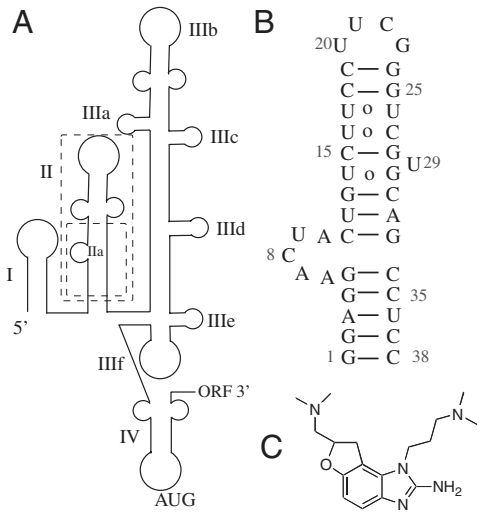

Fig. 1. IRES region of HCV genomic RNA. (*A*) Consensus secondary structure of the HCV IRES RNA (8). Domain II is outlined in the large dashed box, and subdomain IIa in the smaller dashed box. (*B*) Sequence and secondary structure of the RNA construct used for NMR. A UUCG tetraloop sequence was used to promote folding. The bulge nucleosides from A6–A10 (corresponding to residues 53–57 of the full length IRES) of domain IIa result in an approximately 90° bend in the helix trajectory. (*C*) The small-molecule inhibitor, Isis-11.

correlation spectroscopy (TOCSY) NMR experiment provides a map of the U and C residues that have altered environments in the complex; the changes in cross-peak positions suggest that the structure of the bulge is dramatically changed. In the free RNA, U9 and U29 are proximal and both are solvent exposed. The linewidths of the U29 H5 and H6 protons remain narrow in the complex with a strong TOCSY cross-peak, suggesting that U29 remains extruded from the helix. The U29 H5/H6 chemical shift changes suggest that the interaction with neighboring bases is only slightly altered in the complex. In comparison, the U9 TOCSY cross-peak shows a larger change and is significantly broadened due to exchange between the environments for the free RNA and the complex. The large downfield shift of 0.6 ppm for both the H5 and H6 protons of C8 is qualitative support for a structural change wherein C8 becomes less stacked

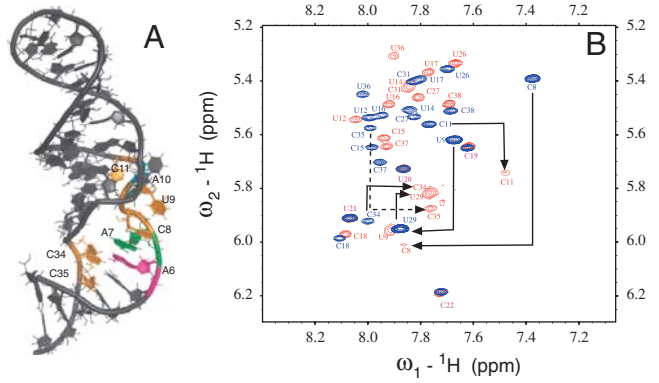

Fig. 2. Chemical shift perturbation of Isis-11 binding. (*A*) The free domain IIa RNA model built from the structure of Lukavsky et al. (12) was refined with CH RDC restraints. Residues C8, U9, C11, C34, and C35 are highlighted in orange and correspond to the pyrimidines with the greatest TOCSY cross-peak changes. Residues A6, A7, and A10 are magenta, green, and cyan, respectively. (*B*) 2D TOCSY NMR spectrum showing pyrimidine base H5–H6 cross-peaks in the absence (blue) and in the presence (red) of a 7-fold excess of Isis-11. Pyrimidine residues experiencing large chemical shift changes are predominantly localized to the bulge region, whereas residues in the stems and the tetraloop (C18, C19, U20, U21, C22) are largely unaffected.

in the complex. There is a corresponding decrease in peak intensity due to the exchange broadening associated with this large chemical shift change.

The extent of the chemical shift changes for residues C8, U9, C11, C34, and C35 indicates that the structure of the bound RNA is different from that of the free RNA, consistent with the RNase A protection results (9). Purine residues in the bulge region also showed large chemical shift changes for H8–C8 cross-peaks in ^{1}H-^{13}C heteronuclear single quantum correlation (HSQC) NMR spectra (Fig. S1). Residues in the two stem regions are less affected, and chemical shift changes did not propagate into the UUCG tetraloop. Well-defined sequential NOE connectivity in the free RNA is seen for residues G5–C8, whereas this connectivity is disrupted in the complex. In contrast, NOEs consistent with a transition to an A-form, stacked arrangement are seen for residues U9–C11 and the lack of H1′–H2′ TOCSY peaks (H1′–H2′ NOESY cross-peaks are observed) for A10 and C11 indicate these residues have mostly 3′-endo sugar conformations (13). The H2–C2 aromatic ^{1}H-^{13}C HSQC cross-peak positions of A6, A7, and A10 are all perturbed in the complex. The changes in NOE connectivity suggest reorganization of the loop structure, but the imino spectral region reporting on base-pairing relationships is remarkably similar for the complex, again consistent with inhibitor binding localized to the bulge. Fluorescence spectroscopy of 2-aminopurine-labeled RNAs (vide infra) provided further verification that inhibitor binding selectively affects the structure of the bulge region, consistent with previous studies of inhibitor binding to domain IIa constructs containing the bulge and upper stem motifs (9).

A Global Structural Change for the RNA Complex. The racemic mixture of the inhibitor was used for the NMR studies, and a model based on the free RNA structure of Lukavsky et al. (12) was used as a starting structure. The inhibitor in the S configuration was randomly oriented in space and then associated with the RNA using low-temperature MD in Xplor-NIH with NOE restraints. Initial structures for the complex were then refined by restrained MD in vacuo with NOE, base-pairing, and dihedral angle restraints (referred to hereafter as "NOE-only" restraints) to generate 20 structures. Of the 20, approximately half belonged to a general consensus family with an rmsd of approximately 4 Å and a low number of NOE violations. The poor global fit was expected due to the sparseness of sequential NOEs for the bulge residues and because RDC restraints were omitted at this stage. Several representatives from this family were then used independently as starting structures for refinement with NOE-only plus RDC restraints. After confirmation that each of these starting structures provided a similar family of 10 structures from the MD refinement, one of the NOE-only refined RNA structures was used to generate a family of 30 complex structures for each of the Isis-11 enantiomers using NOE-only plus RDC restraints. From these families of structures, 16 (R isomer) and 19 (S isomer) lowest energy structures were refined by longer time scale restrained MD at both 300 and 335 K with explicit solvation in AMBER (for details see Table S1 and *SI Text*). For each model, the approximately 15 ns length MD trajectories were clustered at 1 ps intervals into five groups based on the pairwise rmsd of all atoms of the RNA and Isis-11, and the average structure from the dominant cluster at the end of the simulation was minimized with restraints and a generalized Born implicit solvent model. Further energetic analysis (Table S1) of the minimized cluster average and free-energy based ranking of the chosen cluster from the MD trajectory was used to prune the entire set of 35 model structures down to 10 final structures for each of the R and S isomers (Fig. 3*A* and Table S2). Pairwise rmsds are 1.7 and 2.2 Å for the R and S isomers, respectively. The R-isomer structures tend to have fewer bond and torsion violations, lower free energies for the RNA plus Isis-11 complex, and more

favorable RNA free energies. Greater convergence to a common structure was also seen with the R isomers. However, the free energy of binding of Isis-11, estimated from both experiment and simulation, is comparable between the two isomers.

The helical axis of the RNA in the complex is remarkably straight in contrast to the bent structure of the free RNA. Fig. 3*B* shows a comparison of the free RNA and the complex. The free RNA has the characteristic bend produced by the bulge, causing the lower A-form stem to project at an approximately 90° angle away from the lower stem of the complex (12). Not surprisingly, we found both NOE and RDC restraints were necessary for obtaining a well-defined global structure. In addition, greater structural convergence was seen after longer MD simulations with restraints in explicit solvent, even for the less dynamic regions. In Fig. 3*C*, experimental C–H RDC values (Table S3) for the complex are plotted against calculated values for the free RNA and for a representative complex structure. Although there is an excellent correlation for the complex because the RDCs were used to determine those structures, the experimental values are poorly correlated with RDCs calculated from the free RNA. Likewise, the RDC values we measured for the free RNA fit the starting structure extremely well, whereas the free RDCs are poorly correlated with the complex structure (Fig. S1).

Inhibitor Binding and Repacking of the Domain IIa Bulge. At an RNA concentration of 0.4 mM with an excess of inhibitor, we are many-fold above the high-salt K_D of approximately 10 μM (Fig. S2). Therefore, intermolecular NOEs reflect contributions from both of the stereoisomers. Negative ($\omega\tau_c > 1$) Isis-11 intramolecular NOEs were seen among protons of each of the aliphatic side chains, but no NOEs were observed between the two dimethyl-amino side chains, showing that the Isis-11 isomers bind in an extended conformation. There were extensive NOE contacts from protons on the furan attached side chain to both H8 and H1′ of G5, H8 and H1′ of G4, and both H2 and H8 of A6 (Fig. S3). The H8 proton of A7, but not the H2 proton, gave NOEs to the methyl protons of the furan connected chain, whereas no NOEs were seen from residues A6 or A7 to protons on the long chain. The longer side chain showed no NOE connectivity to the lower stem, but the methyl groups on that amino group gave NOEs to the H5 protons of C11 and U12 placing that dimethylamino group in the major groove near these two base-paired pyrimidines. In addition to upper bound restraints from observed NOEs, a lesser number of lower bound intermolecular restraints were included based on resolved RNA protons in the binding pocket that failed to show NOEs to Isis-11 (Table S2).

Isis-11 has a single stereocenter at C11, resulting in two enantiomers that could have different affinities for the HCV RNA. Because it was not possible to experimentally distinguish NOEs arising from either enantiomer specifically, we initially used the quality of fits to the NMR data and energetic results from independent MD simulation runs in an attempt to ascertain which isomer might bind preferentially. Surprisingly, structures of the RNA complexes for both isomers are similar, and the binding modes for each isomer are very similar (Fig. S4). We hypothesize that both the S and R isomers interact favorably with the RNA based on the similarity of the RNA structures with either enantiomer bound, and on the similar binding free energies. The superimposed binding mode was unexpected, but each structure fits the NMR data with low total energy and few experimental violations. These results show that a detailed analysis of molecular simulation runs can provide structural insight in cases of ambiguous primary NMR data. Intermolecular NOE restraints were effective at restricting the positions of the methyl groups and the aliphatic side chains for either of the Isis-11 isomers, but the position of the aromatic group within the RNA structures is more dynamic. NOEs were observed from the A6 H2 proton to the Isis-11 H1/H2 aromatic ring protons, the chiral proton, and the amine methyl groups on the short chain; an observation inconsistent with a single static structure. Generous upper bound restraints were utilized for most of the intermolecular restraints in recognition that the NOEs are averaged by exchange and by the presence of both isomers.

The crucial question of whether the predicted similarity of binding modes could be confirmed experimentally was addressed by small-scale separation of the Isis-11 isomers using chiral HPLC. Titration of 2-aminopurine labeled RNA with each of the purified isomers (Fig. S5) resulted in measured K_D values of 9.0 and 2.6 μM for isomer 1 and isomer 2, respectively. Unfortunately, there is no simple way to relate the HPLC elution

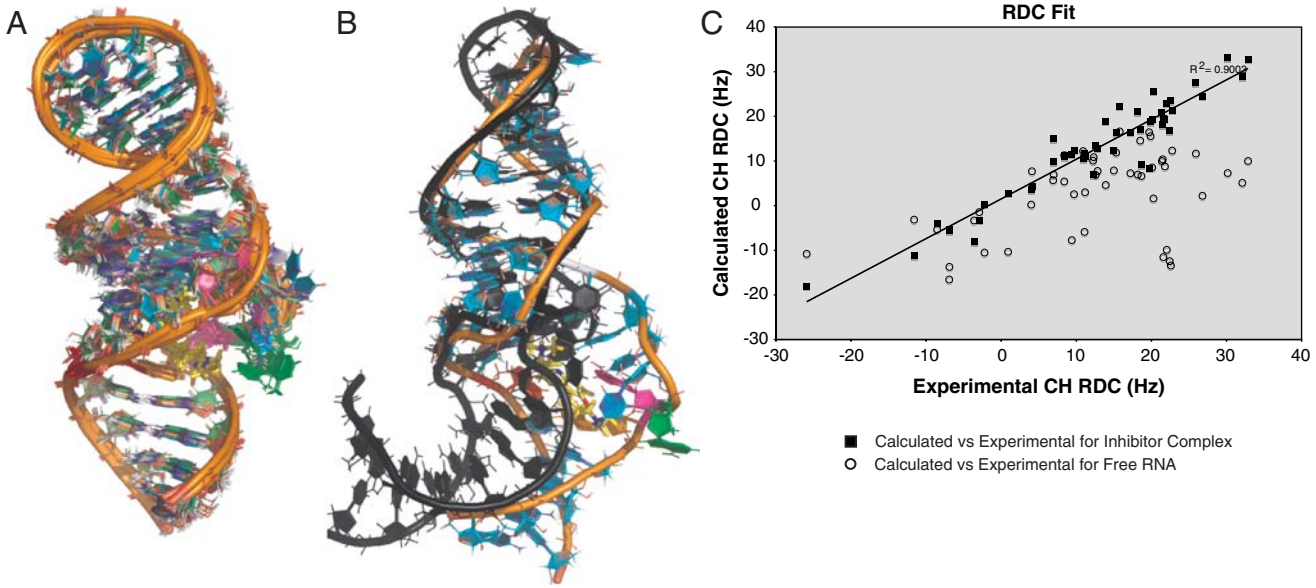

Fig. 3. NMR structures and RDC data. (*A*) Superposition of 10 S-isomer structures from 15 nsec AMBER trajectories. RMSD = 2.3 Å. (*B*) The free RNA model (black) is shown superimposed (residues 12:19, 24:32) on the complex structure (orange backbone) illustrating the change in the helical axis. The inhibitor is shown in yellow. (*C*) RDC fit. CH RDCs were calculated from a representative final complex structure and from the free RNA starting structure; each set of calculated RDCs is plotted against the experimental RDC set for the complex. Filled squares are for the complex, and open circles for the free RNA.

order to the R/S stereochemical configuration. The K_D values are consistent with previous measurements for the racemic mixture, and with the value of 10 ± 20 μM estimated for the racemate from the NMR titration in high salt (Fig. S2).

Previous structural studies showed that magnesium stabilizes the bent conformation of domain IIa (11, 12). The two dimethylamino groups of the inhibitor replace two discrete metal ions characterized by x-ray crystallography, with the amine nitrogens positioned close to each of the previously characterized metal sites (11). The benzimidazole ring serves as a rigid linker for the two dimethylamino chains and directly contributes to RNA binding via extensive π-stacking with G5 and partial stacking with A6. The primary amino group and possibly the dimethylamino group on the furan ring are positioned for cation-π interactions with nucleobases (Fig. S6). To maintain the dimethylamino interactions and to accommodate the benzimidazole within the RNA, the purine bases stacked within the bulge of the free RNA become displaced in the complex, effectively straightening the helix axis (Fig. 4). The benzimidazole aromatic ring stacking onto G5 results in a 1 ppm upfield shift of both Isis-11 aromatic protons in the bound state compared to the positions in the free inhibitor. The chiral (H11) proton is likewise shifted upfield by 1 ppm in the complex as a result of stacking with A6, although the R isomer likely experiences less of a ring current because the chiral proton is oriented away from A6 in the R structures. Direct stacking of A6 over the chiral S proton is seen for only a few structures, however, and never observed for the R isomer structures (Fig. S6). Because of the large chemical shift difference for aromatic and chiral protons between the free and bound states, they are in slow chemical exchange as shown by strong cross-peaks in both NOESY and ROESY NMR experiments, with the characteristic "positive" sign of the ROE cross-peaks relative to the diagonal clearly establishing them as exchange mediated (14). All other RNA and inhibitor NMR resonances display characteristics of fast exchange. The chemical shift of the G5 H8 proton has little change from the free RNA, indicating that the shielding by A6 in the free RNA is replaced by shielding from the benzimidazole aromatic ring in the complex.

Electrostatic Effects on Inhibitor Interactions. Counterion neutralization of the phosphate backbone is a general property of RNA, and electrostatic calculations show that regions remote from the phosphates are typically the most negatively charged. This counterintuitive RNA characteristic can provide binding "hot spots" for positively charged functional groups (15). The electrostatic potential surface of the domain IIa complex was calculated for the RNA alone and for the RNA with bound ligand (16). The two dimethylamino groups are both located near regions of relatively negative electrostatic potential, with the furan chain amino group located in a fairly deep negative pocket (Fig. 4*C*). Despite

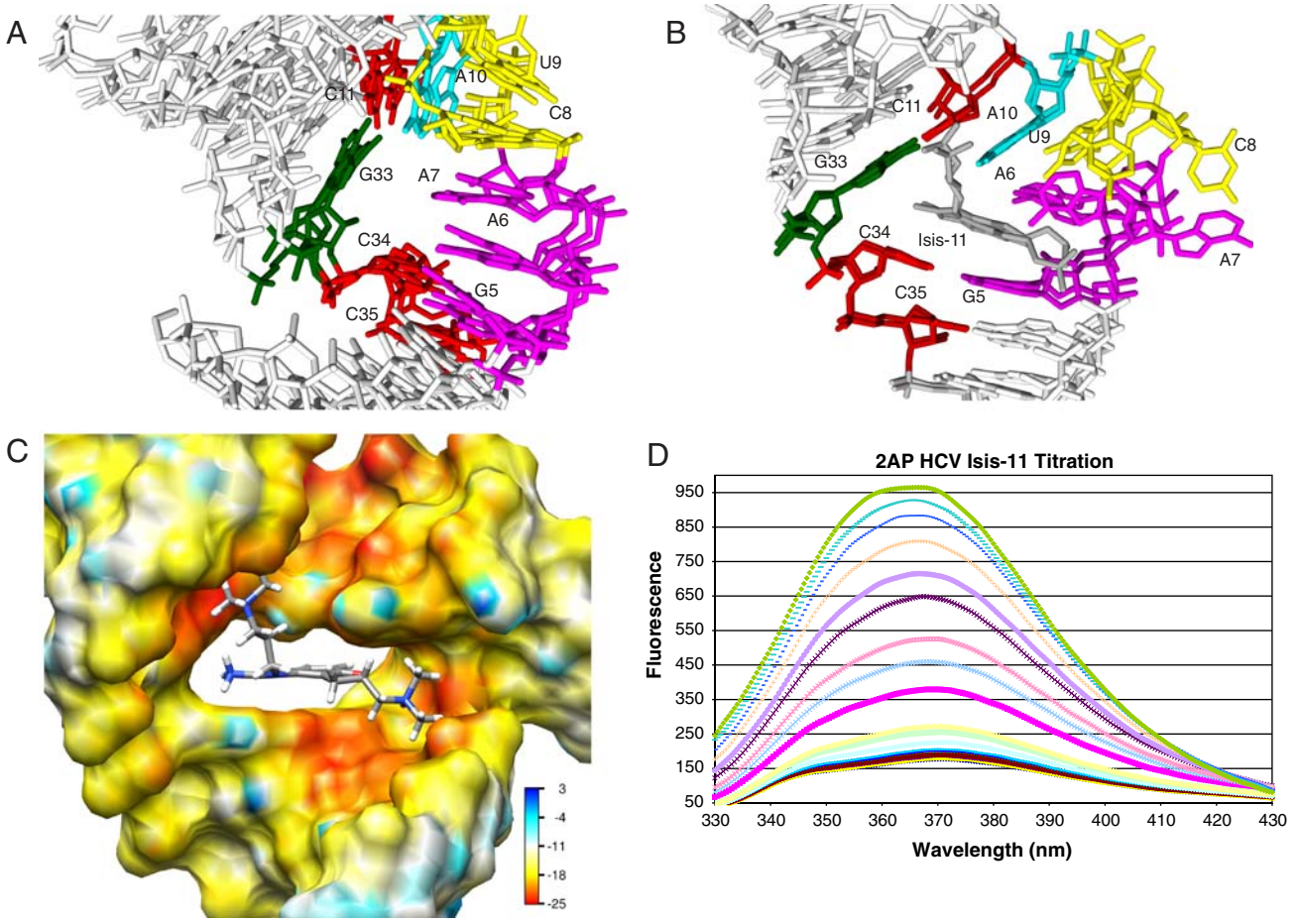

Fig. 4. Base stacking changes in the bulge region of domain IIa. (*A*) Molecular graphics of the heavy atoms of the free RNA using the first three models from PDB 1P5M. (*B*) Isis-11 bound RNA structures (the two lowest energy water-refined NMR structures from each stereoisomer). Residues whose environment changes upon binding are labeled and colored (C11, C34, C35: red; C8, U9: yellow; G5, A6, A7: magenta; A10: cyan; G33: green; Isis-11: gray). The structures were fit using residues 5–11, 33–34 for the free structure and residues 5, 10, 11, 33, 34 for the bound structure. (*C*) electrostatic potential surface calculated for the RNA only using the structure of the complex. Areas of highest negative charge are indicated by the more red colors and are localized near the dimethylamino groups. (*D*) Fluorescence intensity increase for 2AP-6 substituted RNA (1 μM) as a function of inhibitor concentration (see Fig. S5). Emission at 370 nm was fit to a two-state binding model providing a calculated $K_D = 2.4$ μM, comparable to the value previously determined by mass spectrometry.

the structural differences between the free and inhibitor-bound RNAs, it is apparent that a region of negative potential is maintained in the same region where divalent metal ions are observed for the free RNA. Magnesium addition causes clear changes in the imino spectra of the free RNA. However, addition of magnesium to the inhibitor complex causes no change in comparison to the inhibitor complex alone. The T_m of the inhibitor complex under low monovalent salt conditions (10 mM NaCl+ 10 mM KCl) is increased by 12 °C upon addition of 1 mM magnesium, approximately the same change seen when Mg^{2+} is added to the free RNA (11). Although this could indicate that magnesium binds specifically to the complex, the NMR spectra are unaffected by magnesium, and T_m increases of this magnitude are consistent with nonspecific divalent metal binding (17). In high salt conditions, the baseline T_m was too high to accurately measure any further stabilization with added magnesium.

Fluorescence Titrations Are Correlated with Structural Changes. As an independent probe of the change in structural environment for adenosine residues 6, 7, and 10, RNA molecules with 2-aminopurine (2AP) at these positions were synthesized, and the fluorescence emission monitored as a function of added Isis-11 inhibitor. A comparison of the extent of stacking for these adenosines is shown in Fig. 4. The fluorescence for the RNA molecule with 2AP at position 6 is almost completely quenched for the free RNA as a consequence of that adenosine being stacked between purines G5 and A7. Addition of Isis-11 results in a large increase in fluorescence consistent with the structural change (Fig. 4*D*). The adenosine at position 7 also moves from a stacked to an unstacked environment as indicated by an increase in fluorescence emission, whereas A10 becomes more stacked in the complex, consistent with an observed decrease in fluorescence emission of 2AP-10 RNA when the inhibitor is added. Hermann and coworkers recently reported an increase in fluorescence for 2AP-7 RNA (residue 54 in the native numbering scheme) upon binding of a benzimidazole inhibitor related to Isis-11 (18). The AP-6 RNA fluorescence responses upon Isis-l1 isomer addition and for the racemate titrations were fit to two-state binding models, consistent with a single high-affinity binding site.

Conclusions

Domain II of the HCV IRES has a crucial function in cap-independent translation initiation as the apical hairpin loop functions with eIF5 to facilitate eIF2a-GTP hydrolysis, leading to eIF2a-GDP release and subsequent 80S ribosomal assembly (Fig. 5) (5, 7, 19). Conserved nucleotides within the domain IIa bulge induce an approximately 90° bend, resulting in an overall L shape for the entire IRES that is conserved among related viral IRESes (5, 19). The HCV inhibitor Isis-11 binds specifically to the domain IIa bulge and effects a major structural reorganization, causing the 5′ stacked residues to be extruded, and concomitantly promoting new stacking interactions on the 3′ side of the bulge with U9 and A10 stacked onto the C11-G33 base pair. The NMR RDC fits show that the helical regions on either side of the inhibitor binding pocket become coaxial; for the full length IRES this would orient the domain II apical loop away from the ribosomal E-site where eIF5 binds the 40S subunit.

The structural reorganization evident in the NMR structures is supported by characteristic changes in fluorescence intensity for RNAs with 2-aminopurine at each of the three adenosine residues in the bulge region. Fluorescence resonance energy transfer along with 2AP fluorescence was used by the Hermann laboratory to show that another compound of this inhibitor class [compound 13 in the Seth et al. paper (9)] causes a conformational change consistent with straightening of the helical axis (18). The inhibitor they chose has both of the dimethylamino aliphatic side chains incorporated into rings. Compared to Isis-11, it showed slightly higher affinity for the domain II screening target, although it is less potent in cell culture as an HCV replication inhibitor (9). It is clear that both Isis-11 and Isis-13 bind the domain IIa bulge region, resulting in the RNA structural reorganization we have described.

Crucial functional groups of the Isis-11 inhibitor include the two dimethylamino groups that interact with the RNA near the two distinct divalent metal sites seen in crystal structures. These interactions, aromatic stacking of the aminobenzimidazole ring upon G5, and potential cation-π interactions drive inhibitor binding. An aromatic linker does seem to be quite important as we observed that the polyamine spermine does not compete with Isis-11 for the high-affinity site. Moreover, simple model building exercises indicate that the observed binding mode will accommodate related active analogues and fragments (9). There is both experimental and empirical support indicating that the overall RNA stability is relatively unaffected by inhibitor binding. Thermal melting measurements show that addition of the inhibitor decreases the thermal melting transition by 1 °C, with a hyperchomicity difference from 25–80 °C of 14% and 16% for the free RNA and complex, respectively. These small changes are consistent with the structures wherein the base-pairing pattern—as indicated by the imino region of the NMR

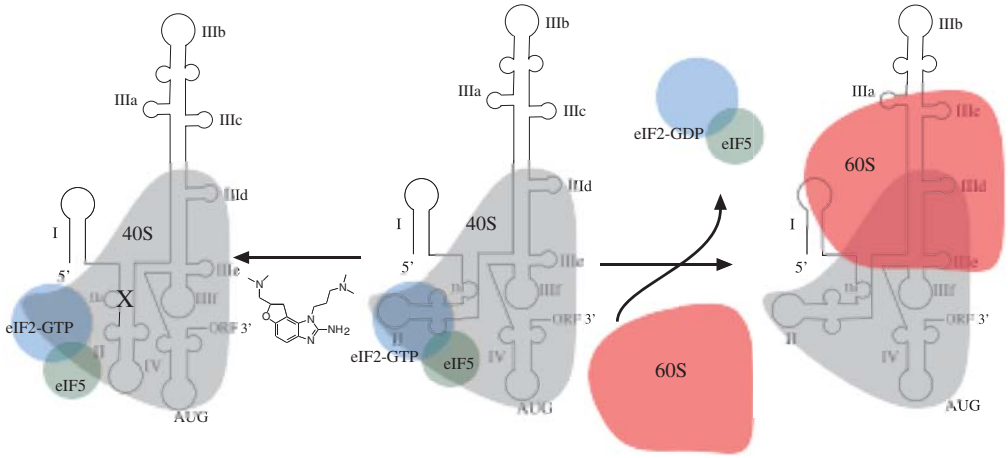

Fig. 5. Model for domain IIa function in 80S ribosomal assembly. (*Center*) Domain IIa of the HCV IRES has a 90° bend that positions the apical loop of domain II in contact the 40S subunit near the E-site, and along with eIF5, promotes hydrolysis of eIF2-GTP and subsequent release of eIF2-GDP. (*Right*) The release of eIF2-GDP allows recruitment of the 60S subunit and eIF3 release to assemble a translation competent 80S ribosome. (*Left*) The inhibitor (X) would straighten IRES domain II, reduce the eIF2-GTP hydrolysis rate, and slow 80S assembly.

spectra—in the free and bound structures is the same. Although there is a significant loss of base stacking for A6, A7, and C8 upon binding, residues U9 and A10 that were unstacked in the free RNA became well-stacked in the complex, as indicated by fluorescence quenching of 2AP-10. These compensatory stacking changes and the maintenance of base-pairing suggest that there is little free energy cost for the RNA despite the dramatic structural change.

The inhibitor binds with low micromolar affinity despite lacking any specific hydrogen bonding interactions; this suggests to us that there is considerable potential for further optimization of this inhibitor class. Tight-binding RNA ligands such as riboswitch effectors make use of a network of hydrogen bonding interactions in addition to base stacking (20). Adding functionality may provide additional RNA contacts, increase the affinity and specificity, and ultimately provide a new class of highly potent and specific HCV therapeutics. The structure we have presented expands our perception of the types of compounds and interactions that can be used to alter RNA structure. It shows that an inhibitor with micromolar RNA affinity can induce a major structural change in the HCV IRES domain IIa RNA, suggesting that a change in IRES structure is the mechanism for HCV replication inhibition.

Materials and Methods

Sample Preparation. RNA molecules were synthesized by in vitro T7 polymerase transcription from synthetic DNA oligonucleotides having two 2′-O-methyl nucleotides at the 5′ terminus of the template strand (21, 22). Isotopically labeled NTPs were purchased from Cambridge Isotope Laboratories and Isotec. NMR samples were made in 10 mM phosphate buffer, pH 7.0 containing 150 mM NaCl, 150 mM KCl, and 2 mM spermine at an RNA concentration of 0.4 mM. Weakly aligned samples were prepared by redissolving lyophilized samples in 250 μL of NMR buffer with either 10% or 100% D_2O containing 3% of C12E5/n-hexanol alignment media, resulting in a ^2H splitting of approximately 13 Hz at 31 °C (23).

NMR Spectroscopy. NMR data were acquired on 500, 600, and 800 MHz Varian NMR spectrometers using RNA optimized pulse sequences from the standard Varian Biopack pulse sequence library (www.varianinc.com). The F1-filtered/F2-filtered NOESY was as described by Zwahlen et al., the F1-filtered/F2-edited NOESY as described by Stuart et al., and the F1-edited/F2-edited NOESY was run as a 2D version of the 4D-^{13}C-edited NOESY of Vuister et al. (Fig. S3) (24–26).

Structure Calculation. Structures were calculated using both Xplor-NIH 2.18 for in vacuo refinement and AMBER 10 for refinement with explicit solvation (*SI Text*). The refinement protocol for simulated annealing in torsion angle space described by Clore and Kuszewski for the RNA aptamer/theophylline complex and provided in the Xplor-NIH distribution was used with only minor changes (27). Alignment tensor calculations were done with either the calcTensor python script provided with Xplor-NIH, or with PALES (28). Electrostatic potential surface calculations were done using the AMBER/APBS module (16). Energetic properties and estimates of the free energy of binding were calculated with AMBER 10 (29, 30).

ACKNOWLEDGMENTS. This work was supported in part by a grant from the US-Israel Binational Science Foundation to D.R.D. The National Institutes of Health (NIH) supported T.E.C. (R01-GM081411) and NMR instrumentation at Utah and at Colorado. The W.M. Keck Foundation supported the 800 MHz NMR at Colorado. Computer time for the MD simulations came from a National Science Foundation award to T.E.C. (MCA01S027) and also local computer time at the Center for High Performance Computing (NIHS10-RR-17214).

1. Robertson B, et al. (1998) Classification, nomenclature, and database development for hepatitis C virus (HCV) and related viruses: Proposals for standardization. International Committee on Virus Taxonomy. *Arch Virol* 143:2493–2503.
2. Manns MP, et al. (2007) The way forward in HCV treatment—Finding the right path. *Nat Rev Drug Discovery* 6:991–1000.
3. Rinaldi A (2006) The phantom menace. *EMBO Rep* 7:14–17.
4. Jang SK (2006) Internal initiation: IRES elements of picornaviruses and hepatitis c virus. *Virus Res* 119:2–15.
5. Locker N, Easton LE, Lukavsky PJ (2007) HCV and CSFV IRES domain II mediate eIF2 release during 80S ribosome assembly. *EMBO J* 26:795–805.
6. Spahn CM, et al. (2001) Hepatitis C virus IRES RNA-induced changes in the conformation of the 40s ribosomal subunit. *Science* 291:1959–1962.
7. Pestova TV, de Breyne S, Pisarev AV, Abaeva IS, Hellen CU (2008) eIF2-dependent and eIF2-independent modes of initiation on the CSFV IRES: A common role of domain II. *EMBO J*.
8. Zhao WD, Wimmer E (1998) Genetic analysis of a poliovirus/hepatitis C virus chimera: New structure for domain II of the internal ribosomal entry site of hepatitis C virus. *J Virol* 75:3719–3730.
9. Seth PP, et al. (2005) SAR by MS: Discovery of a new class of RNA-binding small molecules for hepatitis C virus: Internal ribosome entry site IIa subdomain. *J Med Chem* 48:7099–7102.
10. Williamson JR (2000) Induced fit in RNA-protein recognition. *Nat Struct Biol* 7:834–837.
11. Dibrov SM, Johnston-Cox H, Weng YH, Hermann T (2007) Functional architecture of HCV IRES domain II stabilized by divalent metal ions in the crystal and in solution. *Angew Chem Int Ed* 46:226–229.
12. Lukavsky PJ, Kim I, Otto GA, Puglisi JD (2003) Structure of HCV IRES domain II determined by NMR. *Nat Struct Biol* 10:1033–1038.
13. Varani G, Tinoco I (1991) RNA structure and NMR spectroscopy. *Q Rev Biophys* 24:479–532.
14. Davis DG, Bax A (1985) Separation of chemical exchange and cross-relaxation effects in two-dimensional NMR spectroscopy. *J Magn Reson* 64:533–535.
15. Davis B, et al. (2004) Rational design of inhibitors of HIV-1 TAR RNA through the stabilisation of electrostatic "hot spots". *J Mol Biol* 336:343–356.
16. Baker NA, Sept D, Joseph S, Holst MJ, McCammon JA (2001) Electrostatics of nanosystems: Application to microtubules and the ribosome. *Proc Natl Acad Sci USA* 98:10037–10041.
17. Dove WF, Davidson N (1962) Cation effects on the denaturation of DNA. *J Mol Biol* 5:467–478.
18. Parsons J, et al. (2009) Conformational inhibition of the hepatitis C virus internal ribosome entry site RNA. *Nat Chem Biol* 5:823–825.
19. Spahn CM, et al. (2004) Cryo-EM visualization of a viral internal ribosome entry site bound to human ribosomes: The IRES functions as an RNA-based translation factor. *Cell* 118:465–475.
20. Serganov A (2009) The long and the short of riboswitches. *Curr Opin Struct Biol* 19:1–9.
21. Sherlin LD, et al. (2001) Chemical and enzymatic synthesis of tRNAs for high-throughput crystallization. *RNA* 7:1671–1678.
22. Kao C, Zheng M, Rudisser S (1999) A simple and efficient method to reduce nontemplated nucleotide addition at the 3′ terminus of RNAs transcribed by T7 RNA polymerase. *RNA* 5:1268–1272.
23. Ruckert M, Otting G (2000) Alignment of biological macromolecules in novel nonionic liquid crystalline media for NMR experiments. *J Am Chem Soc* 122:7793–7797.
24. Zwahlen C, et al. (1997) Methods for measurement of intermolecular NOEs by multinuclear NMR spectroscopy: Application to a bacteriophage lambda N-peptide/box B RNA complex. *J Am Chem Soc* 119:6711–6721.
25. Stuart AC, Borzilleri KA, Withka JM, Palmer AG (1999) Compensating for variations in ^1H-^{13}C scalar coupling constants in isotope-filtered NMR experiments. *J Am Chem Soc* 121:5346–5347.
26. Vuister G, et al. (1993) Increased resolution and improved spectral quality in four-dimensional 13C/13C-separated HMQC-NOESY-HMQC spectra using pulsed field gradients. *J Magn Reson Ser B* 101:210–213.
27. Clore GM, Kuszewski J (2003) Improving the accuracy of NMR structures of RNA by means of conformational database potentials of mean force as assessed by complete dipolar coupling cross-validation. *J Am Chem Soc* 125:1518–1525.
28. Zweckstetter M, Bax A (2000) Prediction of sterically induced alignment in a dilute liquid crystalline phase: Aid to protein structure determination by NMR. *J Am Chem Soc* 122:3791–3792.
29. Case DA, et al. (2005) The AMBER biomolecular simulation programs. *J Comput Chem* 26:1668–1688.
30. Srinivasan J, Cheatham TE, III, Cieplak P, Kollman PA, Case DA (1998) Continuum solvent studies of the stability of DNA, RNA and phosphoramidate helices. *J Am Chem Soc* 120:9401–9409.